Journal of Materials Chemistry C

PAPER

View Article Online
View Journal | View Issue

Cite this: J. Mater. Chem. C, 2017, 5, 8390

Excited state properties of non-doped thermally activated delayed fluorescence emitters with aggregation-induced emission: a QM/MM study†

Jianzhong Fan, Lili Lin* and Chuan-Kui Wang*

The excited state properties of dibenzothiophene-benzoyl-9,9-dimethyl-9,10-dihydroacridine (DBT-BZ-DMAC) in the solid phase are theoretically studied through a combined quantum mechanics and molecular mechanics (QM/MM) method. The results indicate that the non-radiative decay rate of the molecule in the solid phase is significantly decreased due to the suppression of the rotation of the DMAC and DBT units in the molecule, while the radiative rate is greatly increased owing to the enhancement of the transition dipole moment. Moreover, the fluorescence efficiency in the solid phase (20.5%) is shown to be much larger than that in the gas phase (0.01‰), which confirms that DBT-BZ-DMAC is a typical aggregation-induced emission (AIE) system. The results further display that both the intersystem crossing (ISC) and reverse intersystem crossing (RISC) processes take place between the first singlet excited state (S1) and the lowest degenerate triplet excited states (T1 and T2). In addition, the charge transfer rate is studied using the Marcus theory and the intrinsic charge mobility is calculated by performing the kinetic Monte Carlo method. The results show that the DBT-BZ-DMAC crystal is a p-type semiconductor with a hole mobility of 0.14 $cm^2\ V^{-1}\ s^{-1}$ at room temperature. Our investigation elucidates the experimental measurements and helps one to understand the AIE mechanisms of the DBT-BZ-DMAC fluorescence emitter, which is beneficial for developing new TADF emitters.

Received 8th June 2017,
Accepted 17th July 2017

DOI: 10.1039/c7tc02541f

rsc.li/materials-c

1. Introduction

Recently, thermally activated delayed fluorescent (TADF) emitters have attracted great attention owing to their potential applications in both full-color flat-panel displays and new generation solid-state lighting. Luminescent materials with thermally activated delayed fluorescence can harvest both singlet and triplet excitons to afford high electroluminescence (EL) efficiencies for organic light emitting diodes (OLEDs) by an efficient reverse intersystem crossing (RISC) process.[1–3] Pioneers such as Adachi *et al.* have reported excellent blue, green and red TADF emitters with external quantum efficiencies (EQEs) of 19.5%, 28.6% and 12.5%, respectively.[4,5] Nevertheless, most TADF molecules have to be dispersed into host matrices to suppress exciton annihilation and concentration or aggregation quenching, which usually results in swift efficiency roll-off as luminance increases, and it becomes an obstacle to device stability and practical applications.[6–8]

TADF molecules with aggregation-induced emission (AIE) characteristics are thought as a promising strategy to solve this problem. AIE is a unique photophysical phenomenon and offers a high possibility to solve the quenching and annihilation problems.[9–11] Usually, AIEgens are weak emitters in dilute solutions, but become highly efficient emitters in a rigid environment such as water or a solid film. Recently, a new tailor-made luminance molecule dibenzothiophene-benzoyl-9,9-dimethyl-9,10-dihydroacridine (DBT-BZ-DMAC) showing both the AIE and TADF properties has been proposed (shown in Fig. 1a). High performance of an OLED has been obtained using the neat film of DBT-BZ-DMAC, which is one of the most efficient non-doped TADF OLEDs.[12]

In this paper, we will perform a detailed study on the photoelectric properties and the AIE mechanism of the DBT-BZ-DMAC molecule based on first-principles calculations. The environmental effect of the molecule in the film is focused by using the combined quantum mechanics and molecular mechanics (QM/MM) method. Because the charge combination ratio γ that influences the external quantum efficiency ($\eta_{EQE} = \gamma\eta_r\eta_{PL}\eta_{out}$) of OLEDs has a close relationship with the charge transfer properties of the molecule in the neat film, we also study both the electron and hole transport properties. The AIE mechanism of the TADF molecule is revealed and the experimental measurements are reasonably elucidated.

Shandong Province Key Laboratory of Medical Physics and Image Processing Technology, Institute of Materials and Clean Energy, School of Physics and Electronics, Shandong Normal University, 250014 Jinan, China.
E-mail: ckwang@sdnu.edu.cn, linll@sdnu.edu.cn

† Electronic supplementary information (ESI) available. See DOI: 10.1039/c7tc02541f

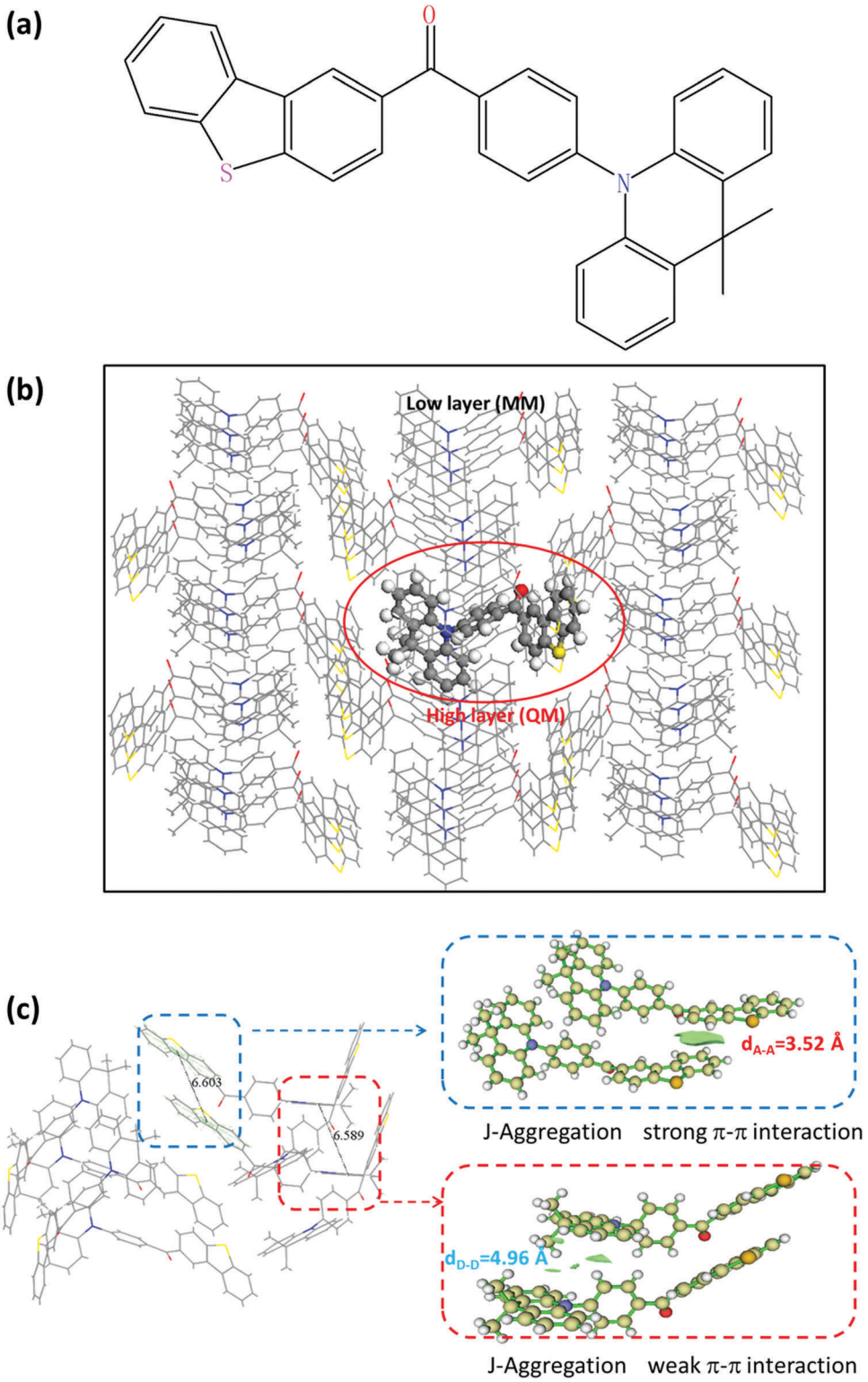

Fig. 1 (a) Chemical structure of DBT-BZ-DMAC. (b) ONIOM model: surrounding molecules are regarded as the low layer and the centered DBT-BZ-DMAC is treated as the high layer. (c) Molecular packing modes of the DBT-BZ-DMAC crystal.

2. Theoretical methods

In this paper, the radiative (K_r) and non-radiative (K_{nr}) decay rates from S1 to S0, the intersystem crossing (K_{ISC}) and reverse intersystem crossing rates (K_{RISC}) between the selected singlet and triplet states are calculated based on first-principles calculations. Further, the fluorescence efficiency $\left(\Phi_{PF} = \frac{K_r}{K_r + K_{nr} + K_{ISC}}\right)$ can

be obtained.[13] Moreover, the charge transfer rate of electrons and holes in the DBT-BZ-DMAC crystal is calculated based on Marcus theory. Then the kinetic Monte Carlo simulation approach is adopted to investigate the charge diffusion process, and further the charge mobility can be acquired.[14,15]

2.1 Excited state properties

The radiative decay rate is calculated as follows

$$K_{\mathrm{r}} = \int \delta_{\mathrm{em}}(\omega, T)\mathrm{d}\omega. \tag{1}$$

where $\delta_{\mathrm{em}}(\omega, T) = \frac{4\omega^3}{3\hbar c^3}\sum_{u,v} P_{\mathrm{i}v}|\langle\Theta_{\mathrm{f}u}|u_{\mathrm{f}i}|\Theta_{\mathrm{i}v}\rangle|^2\delta(\omega_{\mathrm{i}v,\mathrm{f}u} - \omega)$. $u_{\mathrm{f}i} = \langle\Phi_{\mathrm{f}}|\hat{u}|\Phi_{\mathrm{i}}\rangle$ is the electronic transition dipole moment between two electronic states $|\Phi_{\mathrm{f}}\rangle$ and $|\Phi_{\mathrm{i}}\rangle$. $P_{\mathrm{i}v}$ is the initial state Boltzmann distribution function and Θ are the nuclear vibrational wave functions. u and v are vibrational quantum numbers.

The non-radiative decay rate is deduced based on Fermi's golden rule (FGR) and first-order perturbation theory, and it can be written as follows

$$K_{\mathrm{nr}} = \frac{2\pi}{\hbar^2}\sum_{u,v} P_{\mathrm{i}v}\left|H_{\mathrm{f}u,\mathrm{i}v}\right|^2\delta(E_{\mathrm{i}v} - E_{\mathrm{f}u}). \tag{2}$$

The delta function δ maintains the conservation of energy and H is the interaction between two different Born–Oppenheimer states; it contains two components

$$\hat{H}\Psi_{\mathrm{i}v} = \hat{H}^{\mathrm{BO}}\Phi_{\mathrm{i}}(r, Q)\Theta_{\mathrm{i}v}(Q) + \hat{H}^{\mathrm{SO}}\Phi_{\mathrm{i}}(r, Q)\Theta_{\mathrm{i}v}(Q). \tag{3}$$

Here $\hat{H}^{\mathrm{BO}}$ is the nonadiabatic coupling and $\hat{H}^{\mathrm{SO}}$ denotes the spin–orbit coupling. The non-radiative decay rate constant from S1 to S0 can be written as

$$K_{\mathrm{nr}} = \frac{2\pi}{\hbar}\sum_{kl} R_{kl}Z_i^{-1}\sum_{vu}\mathrm{e}^{-\beta E_{\mathrm{i}v}}\langle\Theta_{\mathrm{f}u}|\hat{P}_{\mathrm{f}k}|\Theta_{\mathrm{i}v}\rangle\langle\Theta_{\mathrm{i}v}|\hat{P}_{\mathrm{f}l}|\Theta_{\mathrm{f}u}\rangle\delta(E_{\mathrm{i}v} - E_{\mathrm{f}u}). \tag{4}$$

Here $R_{kl} = \langle\Phi_f|\hat{P}_{fk}|\Phi_i\rangle\langle\Phi_i|\hat{P}_{fl}|\Phi_f\rangle$ is the nonadiabatic electronic coupling. Z_i is the partition function and $\hat{P}_{fk} = -i\hbar\frac{\partial}{\partial Q_{fk}}$ represents the normal momentum operator of the kth normal mode in the final electronic state. As $L_{f\delta j,k} = \frac{\partial q_{\delta j}}{\partial Q_{fk}}$ and $q_{\delta j} = \sqrt{M_\delta}R_{\delta j}$, where $R_{\delta j}$ is the Cartesian coordinate of the δth atom along the jth direction, the electronic coupling term at the equilibrium position can be approximately written as

$$\langle\Phi_f|\hat{P}_{fk}|\Phi_i\rangle = -i\hbar\left\langle\Phi_f\left|\frac{\partial}{\partial Q_{fk}}\right|\Phi_i\right\rangle = -i\hbar\frac{\left\langle\Phi_f^0\left|\frac{\partial U}{\partial Q_{fk}}\right|\Phi_i^0\right\rangle}{E_i^0 - E_f^0}. \tag{5}$$

U is the electron-nuclear potential term in the Hamiltonian. $\left\langle\Phi_f^0\left|\frac{\partial U}{\partial Q_{fk}}\right|\Phi_i^0\right\rangle = -\sum\frac{Z_\delta e^2}{\sqrt{M_\delta}}\sum_{\tau=x,y,z}E_{i\to f,\delta\tau}L_{\delta\tau,k}$, $E_{i\to f,\delta\tau}$ is the transition electric field and it can be calculated using TD-DFT directly. Based on the Franck–Condon principle and applying the Fourier transform of the delta function, the equation can be written as

$$K_{\mathrm{nr}} = \sum_{kl}\frac{1}{\hbar^2}R_{kl}\int_{-\infty}^{\infty}\mathrm{d}t\left[\mathrm{e}^{i\omega_{if}t}Z_i^{-1}\rho_{\mathrm{IC}}(t, T)\right]. \tag{6}$$

Here $\rho_{\mathrm{IC}}(t,T)$ is the thermal vibration correlation function (TVCF).

The intersystem crossing rate constant from initial singlet/triplet to triplet/singlet states can be recast based on the second-order perturbation theory as

$$K_{f\leftarrow i}^{\mathrm{ISC}} = K_{f\leftarrow i}^{(0)} + K_{f\leftarrow i}^{(1)} + K_{f\leftarrow i}^{(2)} \tag{7}$$

For the first-order contribution $K_{f\leftarrow i}^{(0)}$, due to the spin symmetry requirement, the $\hat{H}^{\mathrm{BO}}$ term in eqn (3) does not make any contribution between singlet and triplet states. So, the simplest and the most commonly employed intersystem crossing rate formalism can be written as

$$K_{\mathrm{ISC}} = \frac{1}{\hbar^2}\langle\Phi_f|\hat{H}^{\mathrm{SO}}|\Phi_i\rangle\int_{-\infty}^{\infty}\mathrm{d}t\left[\mathrm{e}^{i\omega_{if}t}Z_i^{-1}\rho_{\mathrm{ISC}}(t, T)\right]. \tag{8}$$

Both the methodology and application of this formalism can be found in Peng's and Shuai's works.[16–18]

2.2 Charge transport properties

To calculate the charge carrier transfer rate from site i to site j, the Marcus–Hush theory is adopted

$$W_{ji} = \frac{V_{ji}^2}{\hbar}\sqrt{\frac{\pi}{K_{\mathrm{B}}T\lambda}}\exp\left[-\frac{(\Delta G_{ji} + \lambda)^2}{4\lambda K_B T}\right]. \tag{9}$$

Here, V_{ji} is the transfer integral between two sites i and j. λ is the reorganization energy between the neutral state and the charge state. ΔG_{ji} is the site energy difference between two sites i and j, and it is defined as $\Delta G_{ji} = E_j - E_i$, with E_i the free energy of site i.

The intrinsic charge mobility can be calculated using the Einstein equation

$$\mu = \frac{eD}{K_{\mathrm{B}}T}. \tag{10}$$

Where D is the diffusion coefficient, and it can be obtained by performing the kinetic Monte Carlo simulations. In the simulations, the crystal structure is adopted and one charge is supposed at one site (one molecule) k first. Then it is transported to another molecule, and it is only allowed to transport to neighbor molecules with the probability as $P_{ki} = \frac{W_{ki}}{\sum_j W_{ki}}$. In the formula, the sum runs over all the possible paths around site k. At each step, one random number r is generated. If the number r satisfies $\sum_{i=1}^{\alpha-1}P_{ki} < r \le \sum_{i=1}^{\alpha}P_{ki}$, then the charge will transport through the α path. By repeating the process for thousands times, the averaged value of the distances with respect to the time follows a linear relationship. The ratio is the diffusion coefficient according to the equation $D = \lim_{t\to\infty}\frac{r^2}{2nt}$, where r and t are the

averaged displacement and total time span and n represents the dimension of the charge transport in the crystal. In our calculation, the $10 \times 10 \times 10$ supercell is adopted, and the limit time for every track is set as 0.01 ns. The average value of the diffusion coefficient D is obtained based on 2000 trajectories. For the detailed simulation method, one can refer to ref. 19.

3. Computational details

The excited states of the DBT-BZ-DMAC molecule are studied using the time-dependent density functional theory (TD-DFT). Since the excited state properties of D-A type molecules are functional dependent, an appropriate functional should be determined firstly. Some ingenious approaches such as the optimal Hartree–Fock (OHF) method, NTO method, LC-wPBE method and LC-BLYP method have been proposed and well applied recently.[20–25] In this work, the emission wavelength of the DBT-BZ-DMAC molecule in gas and solid phases is calculated using functionals with different percentages of HF exchange (HF%). As shown in Table 1, the emission wavelength of the molecule in the solid state calculated with the BMK functional is 490 nm, which is in better agreement with the experimental value (505 nm in the neat film). Consequently, the BMK functional is adopted in our following calculations. For the investigation of the ground state, the DFT method is used. In all the first-principles calculations, the 6-31G(d) basis set is adopted.

In order to simulate the properties of the molecule in the solid state, a combined quantum mechanics and molecular mechanics (QM/MM) method with a two-layer ONIOM approach is used.[26,27] The computational model is built based on the X-ray crystal structure shown in Fig. 1b and the detailed packing structure is shown in Fig. 1c. The central molecule is chosen as the QM section and is set as the high layer, whereas the surrounding 44 molecules are treated as the MM section and are defined as the low layer. The universal force field (UFF) is used for the MM part, and the molecules of the MM part are frozen during the QM/MM geometry optimizations for S0, S1, T1 and T2 states. Besides, the electronic embedding is adopted in the QM/MM calculations by incorporating the partial charges of the MM region into the quantum mechanical Hamiltonian. All the calculations are carried out in the Gaussian 09 package.[28]

Finally, the normal mode analyses are performed using the DUSHIN program,[29] and the radiative and non-radiative decay rates as well as the ISC and RISC rates in gas and solid phases are both calculated in the MOMAP (Molecular Materials Property Prediction Package) which shows superiority in describing and predicting the optical properties of the polyatomic molecules.[30–32]

Table 1 Emission wavelength (nm) calculated by adopting different functionals for DBT-BZ-DMAC in gas and solid phases is listed respectively

	Gas	Solid
O3LYP	709	868
B3LYP	607	677
PBE0	556	614
BMK	454	490
M062X	405	440
wB97XD	391	402
Exp*	—	505

4. Results and discussion

4.1 Geometrical structure

Molecular geometry determines both electronic structures and properties. From the crystal structure of the molecule detected using X-ray, we find two different configurations (shown in Fig. S1, ESI†). In configuratin-1, the C═O bond is above the BZ surface, while it is under the BZ surface in configuration-2 from the view shown in Fig. S1 (ESI†). The DBT units are also in opposite positions in two configurations. Based on the two configurations, we perform optimization in both the gas phase and in the solid phase. The details of structure parameters for both configurations in the ground state (S0), the first excited state (S1) and the first triplet state (T1) are listed in Tables S1 and S2 (ESI†). Comparing the parameters in crystal structures of two configurations, we can see that the dihedral angles of $\theta 2$, $\theta 3$ and $\theta 4$ have the same absolute values but different signs, which indicates different relative positions for three units in two configurations. From the geometric parameters of S0 in the gas phase, the solid phase and the crystal structure, we find that the geometry in the solid phase is closer to the crystal structure. The dihedral angles in the gas phase are significantly different from those in the solid phase, but the angles and bond lengths are almost the same. Since the geometry differences between S0 and S1 have close relationship with the excited state properties, the intuitive comparisons of the geometries of S0 and S1 are shown in Fig. S2 and S3 (ESI†). It is found that the geometric changes between S0 and S1 in the gas phase are more significant than that in the solid phase. To quantitatively characterize the geometric change, the root of the mean of squared displacement (RMSD) between two states is calculated using Multiwfn.[33] The RMSD for configuration-1 in the gas phase is 0.342 Å, while it is only 0.136 Å in the solid phase. For configuration-2, similar variations between S0 and S1 can be found. The different geometric change between S0 and S1 in both phases implies that the change in the geometry in the solid phase is more difficult than that in the gas phase. It also indicates that vibrational relaxation in the solid state will be limited and the non-radiative decay may be suppressed. To confirm our deduction, the energy is scanned when the dihedral angle between BZ and DMAC units in configuration-1 is changed. As shown in Fig. S4 (ESI†), the energy barrier for the molecule in the solid phase is much higher than that in the gas phase. One should note that the rotation angle in the figure is expressed by the dihedral angle after rotation minus the dihedral angle at equilibrium. Besides, the rotational energy barrier (kcal mol^{-1}) is defined as the energy difference between the configuration after rotation and the S0 geometry. The result confirms our deduction that the rotation for the molecule in the solid phase is much more difficult than that in the gas phase. In addition, remarkable dislocated intermolecular π–π interactions (measured by the

reduced density gradient (RDG) function) can be found at DBT units as well as at the DMAC units with a vertical distance of 3.52 Å and 4.96 Å respectively (as shown in Fig. 1(c)). In addition, J-aggregation can be found in the crystal, which can efficiently enhance the emission efficiency of the molecule in the solid phase.[34]

Although there are two configurations for the DBT-BZ-DMAC molecule, we find that there are no significant differences in its electronic properties and other photophysical properties between two configurations except for the geometry and quite a little difference in frequencies. Consequently, the calculations below are only performed based on configuration-1.

4.2 Energy landscape and the transition properties

To analyze the exciton transfer process, the ground and excited states are optimized using the BMK functional with the 6-31G(d) basis set under the DFT and TD-DFT theories respectively. Adiabatic energy landscapes of several low-lying excited states in both gas and solid phases are shown in Fig. 2(a) and (b) respectively. In the gas phase, there are two triplet levels lower in energy than S1. The S1–T1 energy gap is 0.12 eV, and the S1–T2 gap is 0.08 eV. Such small gaps can efficiently promote the RISC process from T1 (T2) to S1. In the solid state, the energy levels of T1 and T2 are degenerate with a S1–T1 (S1–T2) gap of 0.10 eV, which is consistent with the experimental value (0.08 eV).[12]

Moreover, the transition properties of excited states play an important role in determining the excited state properties. Based on the calculations above, we note that the S1, T1 and T2 states have close relationship with the ISC process. As we know, the HOMO–LUMO overlap has direct relationship with the S–T energy gap and also the radiative rate. In Fig. S5 (ESI†), the electronic distribution of the HOMO and LUMO for the DBT-BZ-DMAC molecule in both the gas phase and the solid phase is presented. It can be found that the electrons are mainly located at the DMAC unit in the HOMOs, while they are localized at the BZ and DBT units in the LUMOs in both phases. A separate distribution of the HOMO and LUMO can be found, which is consistent with the small S–T energy gap of the molecule. The oscillator strength for the S1 state of the molecule in the gas phase and the solid phase is 0.0002 and 0.0124, respectively, both of which are smaller than those of the normal fluorescent molecules.

Natural transition orbital (NTO) analysis for S1, T1 and T2 in the gas phase and the solid state are performed respectively (shown in Fig. 3). For the molecule in the gas phase, we find that S1 is a typical charge transfer (CT) state. For T1 and T2, a significant local excitation (LE) feature can be found. In the solid phase, the transition properties of S1 and T2 are similar to that in the gas phase, while the nature of T1 changes to CT transition. It indicates that the environment has an important influence on the transition character of the excited state. Recently, Gibson and Penfold found that ^{3}LE often brings a stable triplet state and ^{3}CT can result a small energy gap between ^{1}CT and ^{3}CT.[35] Nonadiabatic coupling between ^{3}LE and ^{3}CT opens up the possibility for a significant second-order coupling effect and promotes the RISC process.[36,37] Thus an ideal TADF model is proposed, where the ^{3}CT → ^{3}LE → ^{1}CT up-conversion process is beneficial to the up-conversion process. For the DBT-BZ-DMAC molecule, we find that the energy levels and transition characters in the solid state agree well with the ideal model proposed by them and good performance is expected.

4.3 Huang–Rhys factor and reorganization energy

The Huang–Rhys (HR) factor characterizes the modification of vibrational quanta when going from one electronic state to another, and it can be written as $\mathrm{HR}_k = \frac{w_k D_k^2}{2\hbar}$, where ω_k is the vibration frequency and D_k is the normal coordinate displacement of mode k. The HR factors for S1 of the molecule in the gas phase and in the solid phase are depicted in Fig. 4(a) and (b). Representative large HR factors in the gas phase are 10.7 (19.6 cm^{-1}), 1.4 (76.4 cm^{-1}) and 1.1 (122.5 cm^{-1}), which correspond to the rotation of DMAC and DBT units as shown in the insets. While, all the HR factors are decreased in the solid phase with 1.9 (43.4 cm^{-1}) as the largest one. The calculation

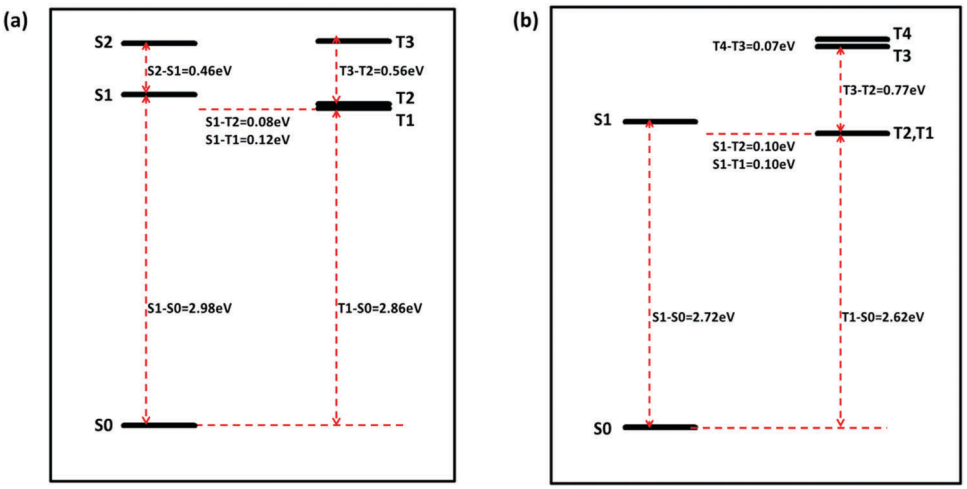

Fig. 2 Adiabatic excitation energies for DBT-BZ-DMAC in gas (a) and solid phases (b) respectively.

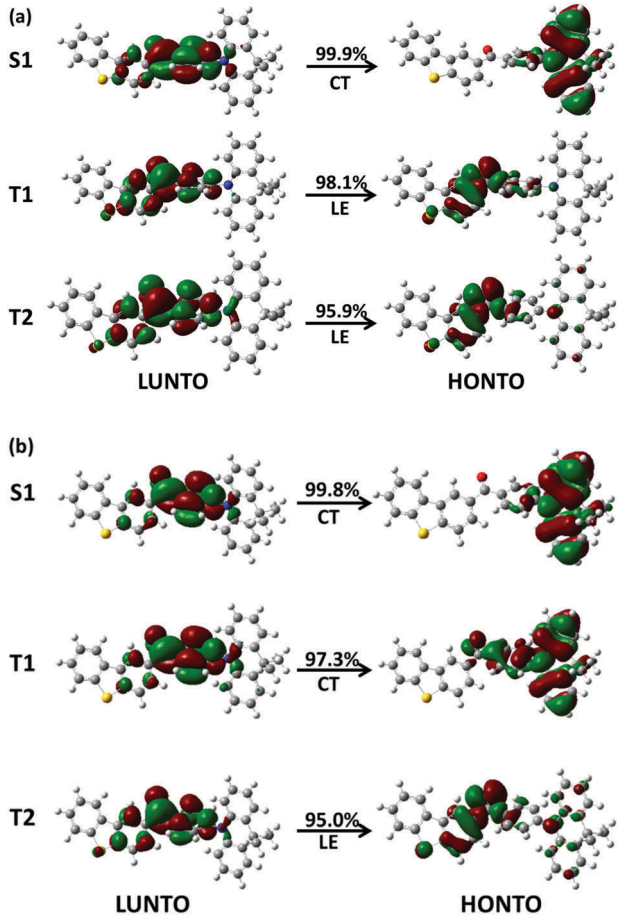

Fig. 3 Transition characteristics for S1, T1 and T2 sates of DBT-BZ-DMAC in gas (a) and solid phases (b) respectively.

results indicate that the rotation motions of DMAC and DBT units in low frequency regions (<200 cm^{-1}) are hindered in the solid phase due to the intermolecular interactions. Thus, the energy dissipation *via* vibration decay can be suppressed due to aggregation and the fluorescent efficiency can be enhanced in the solid phase. Besides, the reorganization energies $\left(\lambda = \sum_k \hbar w_k \mathrm{HR}_k\right)$ *versus* the normal mode frequencies in both phases are shown in Fig. 4(c) and (d). Contribution from the low frequency modes to the total reorganization energies accounts for 24.9% (75 meV) in the gas phase, while the corresponding result decreases to 13.0% (30.1 meV) in the solid phase. It further confirms that the rotation with low-frequencies can be suppressed in the solid phase.

To further understand the relationship between the photophysical properties and the molecular structures, we project the reorganization energies onto the internal coordinate of the molecule. Contributions from bond lengths, bond angles and dihedral angles are demonstrated in Fig. S6 (ESI†), and corresponding data are listed in Table 2. It is noted that the bond lengths (mainly C=O vibration) contribute most to the total reorganization energy (55.6% in gas phase), and it increases to 70.3% in total reorganization energy in the solid phase. However, the contribution from dihedral angles is significantly decreased from 26.6% (80.2 meV) in the gas phase to 14.7% (33.9 meV) in the solid phase. There is also some decrease in the contribution from bond angles. From Table 2, we find that the total reorganization energy in the solid phase (230.6 meV) is smaller than that in the gas phase (301.2 meV) with the decreased energy 70.6 meV from the gas to solid phase, which should mainly due to the decrease in the contribution from dihedral angles ($\Delta_{\text{Gas-Solid}}$ = 46.3 meV). These results further confirm that the rotation of DMAC and DBT units in low frequency regions can be effectively suppressed in the solid phase, and it is also crucial to determine the photophysical properties.

4.4 Excited state properties and aggregation-induced emission

Based on first-principles calculations, the spin–orbit coupling (SOC) constants (with the unit of cm^{-1}) between S1 and two lowest triplet excited states both in the gas phase and the solid phase are calculated using the Dalton2013 package,[38] and the corresponding data are listed in Table 3. It can be found that the SOC constants for the ISC process based on the S1 structure (0.012 cm^{-1} and 0.584 cm^{-1}) are all smaller than those based on T1 (0.355 cm^{-1}) and T2 (2.154 cm^{-1}) for the RISC process. The similar results can be seen in the solid phase. Further, we calculate the radiative (K_r) and non-radiative (K_{nr}) rates from S1 to S0 as well as the ISC (K_{ISC}) and RISC (K_{RISC}) rates between singlet and triplet excited states in both the gas phase and solid phase, and all the calculated results and experimental data are listed in Table 4. It is found that the radiative decay rate K_r is greatly increased in the solid phase (1.32×10^7 s^{-1}), this is due to the enlarged transition dipole moment (1.14 D in solid phase) compared with that in the gas phase (0.13 D). The non-radiative decay rate K_{nr} from S1 to S0 is 4.86×10^9 s^{-1} in gas phase, which is five orders of magnitude larger than K_r (4.82×10^4 s^{-1}). Consequently, weak or no light-emitting can be found for the isolate molecule. Nevertheless, for the molecule in the solid phase, K_{nr} in the solid phase (2.40×10^7 s^{-1}) is decreased about two orders compared with that in the gas phase. It becomes comparable with the radiative decay rate (1.32×10^7 s^{-1}), and efficient light-emitting can be expected. To confirm the reliability of the non-radiative decay rate in our calculations, we plot the $\log K_{nr}(\Delta E$ (eV)) parabola in Fig. S7 (ESI†). No vibrational feature is found in both lines, which indicates the accuracy of the calculated K_{nr} values in gas and solid phases. As a result, the significant decrease of the non-radiative rate in the solid phase is caused by the intermolecular interactions.

Moreover, the ISC and RISC rates between S1 and T1 (T2) are calculated. It is found that the conversion rates between S1 and T2 are larger than the values between S1 and T1 in both the ISC process and the RISC process. This is due to the larger SOC constants and a smaller energy gap between S1 and T2 than that between S1 and T1. The results indicate that both ISC and RISC processes mainly occur between S1 and T2. Besides, an interesting phenomenon is found in the gas phase. The RISC rate (1.84×10^4 s^{-1}) from T1 to S1 is slightly larger than the ISC rate (1.44×10^4 s^{-1}) from S1 to T1, which is because the calculated SOC constant based on T1 (0.355 cm^{-1}) is about 28 times larger

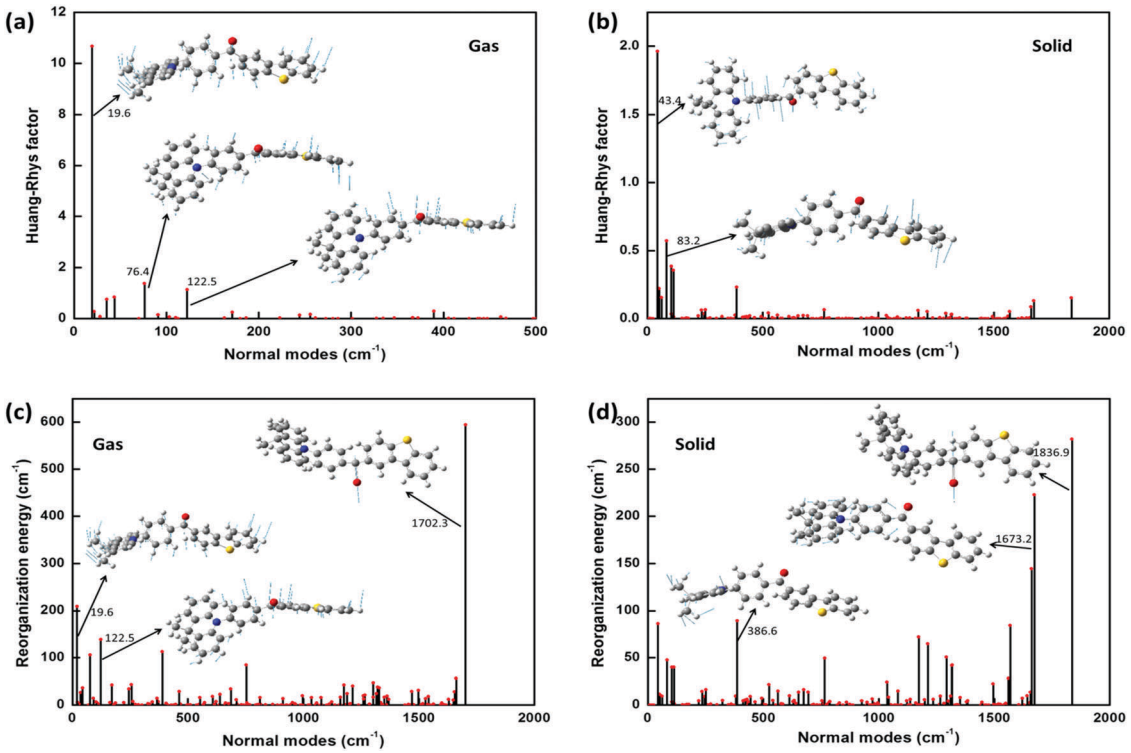

Fig. 4 Calculated HR factors *versus* the normal mode frequencies in gas (a) and solid phases (b) as well as the reorganization energies *versus* the normal mode frequencies in gas (c) and solid phases (d) respectively. Representative vibration modes are shown as insets.

Table 2 Reorganization energies (meV) from the bond length, bond angle, and dihedral angle in gas and solid phases are listed respectively. $\Delta_{\text{Gas-Solid}}$ represents the energy difference between gas and solid phases

	Gas	Solid	$\Delta_{\text{Gas-Solid}}$
Bond length	167.6	162.0	5.6
Bond angle	53.4	34.7	18.7
Dihedral angle	80.2	33.9	46.3
Total	301.2	230.6	70.6

Table 3 Calculated spin orbit coupling constants (cm^{-1}) between selected singlet and triplet excited states for DBT-BZ-DMAC in gas and solid phases, based on the optimized S1, T1 and T2 structures respectively

	Gas		Solid	
Geometry	⟨S1|Hso|T1⟩	⟨S1|Hso|T2⟩	⟨S1|Hso|T1⟩	⟨S1|Hso|T2⟩
S1	0.012	0.584	0.218	0.539
T1	0.355	—	0.545	—
T2	—	2.154	—	1.286

than that based on S1 (0.012 cm^{-1}). A similar situation was also observed in a recent experiment.[39] The calculation results indicate the important role of the SOC in the ISC and RISC processes, one should always combine both the energy landscape and the decay rate to analyze the excited state properties.

To compare with the experimental results, we define effective ISC and RISC rates as: $K_{\text{ISC}}^{\text{cal}}(\text{S} \rightarrow \text{T}) = \dfrac{K_{\text{S1-T1}}{}^2 + K_{\text{S1-T2}}{}^2}{K_{\text{S1-T1}} + K_{\text{S1-T2}}}$ and $K_{\text{RISC}}^{\text{cal}}(\text{T} \rightarrow \text{S}) = \dfrac{K_{\text{T1-S1}}{}^2 + K_{\text{T2-S1}}{}^2}{K_{\text{T1-S1}} + K_{\text{T2-S1}}}$. Based on these formulas,

Table 4 Calculated radiative and nonradiative rates (s^{-1}) from S1 to S0 as well as the ISC and RISC rates (s^{-1}) between singlet and triplet excited states. The calculated prompt fluorescence efficiency (Φ_{PF}) and ISC efficiency (Φ_{ISC}) are listed. Corresponding experimental results are also presented with the superscript 'exp'

	Gas	Solid
$K_{\text{r}}(\text{S1} \rightarrow \text{S0})$	4.82×10^4	1.32×10^7
$K_{\text{nr}}(\text{S1} \rightarrow \text{S0})$	4.86×10^9	2.40×10^7
$K_{\text{ISC}}(\text{S1} \rightarrow \text{T1})$	1.44×10^4	5.62×10^6
$K_{\text{ISC}}(\text{S1} \rightarrow \text{T2})$	1.61×10^6	3.11×10^7
$K_{\text{RISC}}(\text{T1} \rightarrow \text{S1})$	1.84×10^4	2.50×10^4
$K_{\text{RISC}}(\text{T2} \rightarrow \text{S1})$	6.37×10^5	6.59×10^5
$K_{\text{ISC}}^{\text{cal}}(\text{S} \rightarrow \text{T})$	1.60×10^6	2.72×10^7
$K_{\text{RISC}}^{\text{cal}}(\text{T} \rightarrow \text{S})$	6.20×10^5	6.36×10^5
Φ_{PF}	0.01‰	20.5%
Φ_{ISC}	0.03%	42.2%
$K_{\text{r}}^{\text{exp}}(\text{S1} \rightarrow \text{S0})$	—	7.04×10^6
$K_{\text{nr}}^{\text{exp}}(\text{S1} \rightarrow \text{S0})$	—	1.74×10^6
$K_{\text{ISC}}^{\text{exp}}(\text{S} \rightarrow \text{T})$	—	1.60×10^7
$K_{\text{RISC}}^{\text{exp}}(\text{T} \rightarrow \text{S})$	—	7.76×10^5
$\Phi_{\text{PF}}^{\text{exp}}$	—	28.5%
$\Phi_{\text{ISC}}^{\text{exp}}$	—	64.5%

$$K_{\text{ISC}}^{\text{cal}}(\text{S} \rightarrow \text{T}) = \frac{K_{\text{S1-T1}}{}^2 + K_{\text{S1-T2}}{}^2}{K_{\text{S1-T1}} + K_{\text{S1-T2}}} K_{\text{RISC}}^{\text{cal}}(\text{T} \rightarrow \text{S}) = \frac{K_{\text{T1-S1}}{}^2 + K_{\text{T2-S1}}{}^2}{K_{\text{T1-S1}} + K_{\text{T2-S1}}}.$$

$$K_{\text{RISC}}^{\text{exp}}(\text{T} \rightarrow \text{S}) = \frac{K_{\text{TADF}}^{\text{exp}}}{1 - \dfrac{K_{\text{ISC}}^{\text{exp}}}{K_{\text{r}}^{\text{exp}} + K_{\text{nr}}^{\text{exp}} + K_{\text{ISC}}^{\text{exp}}}}.$$

we can obtain the effective ISC and RISC rates as 2.72×10^7 s^{-1} and 6.36×10^5 s^{-1} respectively in the solid phase, which agree

well with experimental values (as shown in Table 4). Based on our calculations in the solid state, the fluorescence efficiency Φ_{PF} is 20.5%, which is consistent with the experimental result (28.5%). The calculated ISC efficiency Φ_{ISC} is 42.2%, which is also comparable with the experimental value (64.5%). Theoretical results based on first-principles calculations in the solid state show good agreement with the experimental results, which confirms the TADF mechanism of the molecule. In addition, comparison of the non-radiative decay rate in the gas phase and in the solid phase also proves that the DBT-BZ-DMAC molecule has significant AIE properties.

4.5 Charge transfer properties

For TADF-OLEDs, the charge transport properties are important factors to determine the external quantum efficiency and efficiency roll-off of the device. Good injection, bipolar and balanced hole and electron transfer in molecular neat films is expected to obtain successful TADF-OLEDs. Experiment shows that the electron transport of the DBT-BZ-DMAC neat film is inferior to those of commercial electron transporting materials such as TmPyPB films, but the hole transport is comparable to those of commercial hole-transporting materials such as CBP and mCP films.[12] A theoretical study on the intrinsic transport properties of the DBT-BZ-DMAC crystals is systematically performed. Based on the crystal data, the dominant charge transfer pathways are shown in Fig. 5. One can see that there are only four effective paths for charge transport. The paths of P1 and P2 play major roles with transfer integrals (V) 15.3 meV and 11 meV in holes and electrons respectively. The transfer integrals along other two paths (P3 and P4) are 6.5 meV for holes and 1.9 meV for electrons. Further, the charge mobility of both holes and electrons can be calculated using the kinetic Monte Carlo simulations. The temperature dependence of the charge mobility is also investigated (shown in Fig. 6). One can see that the hole

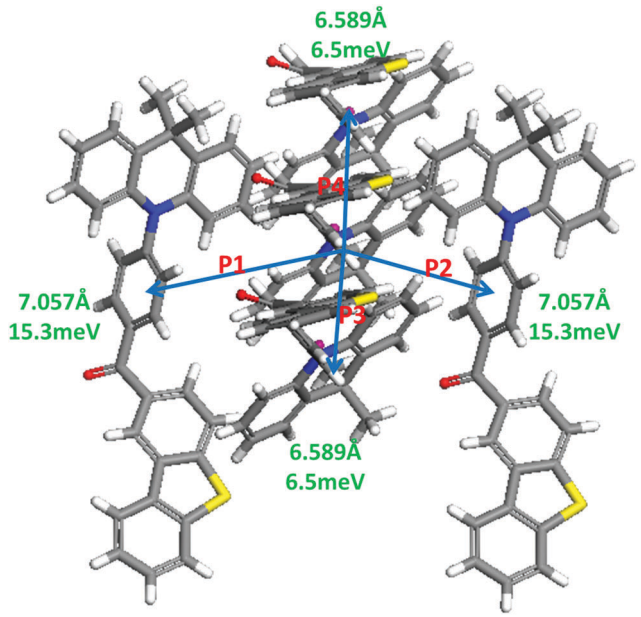

Fig. 5 Main hole-transfer pathways of DBT-BZ-DMAC in the single crystal.

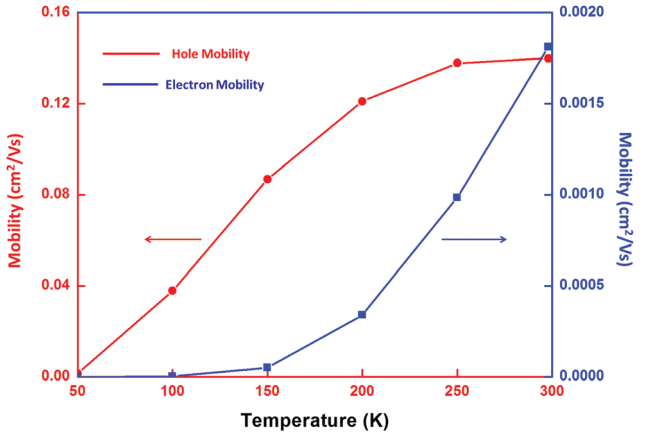

Fig. 6 Temperature dependence of hole (red) and electron (blue) mobility for DBT-BZ-DMAC in the single crystal.

mobilities are all higher in values than electron mobilities in the temperature from 50 K to 300 K, which indicates that the DBT-BZ-DMAC molecular crystal is a typical p-type organic semiconductor with a hole mobility of 0.14 $cm^2\ V^{-1}\ s^{-1}$ in 298 K. Both the hole mobility and electron mobility increase with the temperature, which also confirms the hopping transfer mechanism of charges in the molecular crystal. In addition, the reorganization energies (λ) of holes (155 meV) and electrons (480 meV) calculated by normal mode (NM) analyses are all much larger than their transfer integrals. All these features $\left(\frac{du}{dT} > 0, \lambda \gg V\right)$ indicate a hopping mechanism for the DBT-BZ-DMAC molecular crystal.

5. Conclusion

In summary, the excited state properties of the DBT-BZ-DMAC molecule in the solid state are studied using the QM/MM method. Based on the crystal structures, two kinds of configurations are found for the molecule. First-principles calculations indicate that the energy, electronic structures and photophysical properties are almost the same for the two configurations. The geometric change between the S0 state and the S1 state in the solid phase is much less than that in the gas phase. Moreover, the Huang–Rhys factors and reorganization energies in the solid phase are smaller than those in the gas phase, which is due to the suppression of the rotational motion of the DMAC unit and the DBT unit with low frequencies ($<200\ cm^{-1}$). Thus, the non-radiative rate from S1 to S0 in the solid state is greatly decreased compared to that in the gas phase. All these results indicate the key role of the environmental effect on the molecular properties. Furthermore, enhanced fluorescence efficiency is found in the solid phase (20.5%) compared with that in the gas phase (0.01‰), which results from the AIE mechanism. First-principles calculations combined with the Kinetic Monte Carlo simulations are used to study the charge transport properties in the DBT-BZ-DMAC molecular crystal. The results demonstrate that the DBT-BZ-DMAC molecular crystal is a p-type organic semiconductor with a hole mobility of

0.14 $cm^2 V^{-1} s^{-1}$ at room temperature. Our investigation can help one to understand the TADF and AIE mechanisms of the DBT-BZ-DMAC emitter.

Conflicts of interest

There are no conflicts of interest to declare.

Acknowledgements

This work is supported by the National Natural Science Foundation of China (Grant No. 11374195 and 21403133). The authors thank the support from Taishan Scholar Project of Shandong Province and the Scientific Research Foundation of Shandong Normal University. The authors thank the support from the Promotive Research Fund for Excellent Young and Middle-aged Scientists of Shandong Province (Grant No. BS2014CL001) and the General Financial Grant from the China Postdoctoral Science Foundation (Grant No. 2014M560571). Great thanks to Professor Yi Luo, Professor Zhigang Shuai and Qian Peng for their helpful suggestions in our calculations. The authors thank Professor Yingli Niu for his great help in the usage of MOMAP.

References

1 C. W. Tang and S. A. VanSlyke, *Appl. Phys. Lett.*, 1987, **51**, 913.
2 K. Yoshida, T. Matsushima, H. Nakanotani and C. Adachi, *Org. Electron.*, 2016, **31**, 191.
3 S. Xu, R. Chen, C. Zheng and W. Huang, *Adv. Mater.*, 2016, **28**, 9920.
4 H. Uoyama, K. Goushi, K. Shizu, H. Nomura and C. Adachi, *Nature*, 2012, **492**, 234.
5 Q. Zhang, B. Li, S. Huang, H. Nomura, H. Tanaka and C. Adachi, *Nat. Photonics*, 2014, **8**, 326.
6 J.-X. Chen, W. Liu, C.-J. Zheng, K. Wang, K. Liang, Y.-Z. Shi, X.-M. Ou and X.-H. Zhang, *ACS Appl. Mater. Interfaces*, 2017, **9**, 8848.
7 T. Liu, L. Zhu, C. Zhong, G. Xie, S. Gong, J. Fang, D. Ma and C. Yang, *Adv. Funct. Mater.*, 2017, **27**, 1606384.
8 S. Wu, M. Aonuma, Q. Zhang, S. Huang, T. Nakagawa, K. Kuwabara and C. Adachi, *J. Mater. Chem. C*, 2014, **2**, 421.
9 H. Tsujimoto, D.-G. Ha, G. Markopoulos, H. S. Chae, M. A. Baldo and T. M. Swager, *J. Am. Chem. Soc.*, 2017, **139**, 4894.
10 J. Hu, X. Zhang, D. Zhang, X. Cao, T. Jiang, X. Zhang and Y. Tao, *Dyes Pigm.*, 2017, **137**, 480.
11 L. Q. Yan, Z. N. Kong, Y. Xia and Z. J. Qi, *New J. Chem.*, 2016, **40**, 7061.
12 J. Guo, X.-L. Li, H. Nie, W. Luo, S. Gan, S. Hu, R. Hu, A. Qin, Z. Zhao, S.-J. Su and B. Z. Tang, *Adv. Funct. Mater.*, 2017, **27**, 1606458.
13 Y. Tao, K. Yuan, T. Chen, P. Xu, H. Li, R. Chen, C. Zheng, L. Zhang and W. Huang, *Adv. Mater.*, 2014, **26**, 7931.
14 L. Wang, Q. Li, Z. Shuai, L. Chen and Q. Shi, *Phys. Chem. Chem. Phys.*, 2010, **12**, 3309.
15 L. Lin, H. Geng, Z. Shuai and Y. Luo, *Org. Electron.*, 2012, **13**, 2763.
16 Z. Shuai and Q. Peng, *Phys. Rep.*, 2014, **537**, 123.
17 Q. Peng, Y. Yi, Z. Shuai and J. Shao, *J. Chem. Phys.*, 2007, **126**, 114302.
18 Y. Niu, Q. Peng and Z. Shuai, *Sci. China, Ser. B: Chem.*, 2008, **51**, 1153.
19 Z. Shuai, H. Geng, W. Xu, Y. Liao and J.-M. André, *Chem. Soc. Rev.*, 2014, **43**, 2662.
20 S. Huang, Q. Zhang, Y. Shiota, T. Nakagawa, K. Kuwabara, K. Yoshizawa and C. Adachi, *J. Chem. Theory Comput.*, 2013, **9**, 3872.
21 T. Chen, L. Zheng, J. Yuan, Z. An, R. Chen, Y. Tao, H. Li, X. Xie and W. Huang, *Sci. Rep.*, 2015, **5**, 10923.
22 H. Sun, C. Zhong and J.-L. Bredas, *J. Chem. Theory Comput.*, 2015, **11**, 3851.
23 T. J. Penfold, *J. Phys. Chem. C*, 2015, **119**, 13535.
24 J. Z. Fan, S. Qiu, L. L. Lin and C. K. Wang, *Chin. J. Chem. Phys.*, 2016, **29**, 291.
25 J. Z. Fan, L. L. Lin and C. K. Wang, *Chem. Phys. Lett.*, 2016, **652**, 16.
26 L. W. Chung, W. M. Sameera, R. Ramozzi, A. J. Page, M. Hatanaka, G. P. Petrova, T. V. Harris, X. Li, Z. Ke, F. Liu, H. B. Li, L. Ding and K. Morokuma, *Chem. Rev.*, 2015, **115**, 5678.
27 J. Fan, L. Cai, L. Lin and C.-K. Wang, *J. Phys. Chem. A*, 2016, **120**, 9422.
28 M. J. Frisch, G. W. Trucks, H. B. Schlegel, G. E. Scuseria, M. A. Robb, J. R. Cheeseman, G. Scalmani, V. Barone, B. Mennucci, G. A. Petersson, H. Nakatsuji, M. Caricato, X. Li, H. P. Hratchian, A. F. Izmaylov, J. Bloino, G. Zheng, J. L. Sonnenberg, M. Hada, M. Ehara, K. Toyota, R. Fukuda, J. Hasegawa, M. Ishida, T. Nakajima, Y. Honda, O. Kitao, H. Nakai, T. Vreven, J. A. Montgomery, Jr., J. E. Peralta, F. Ogliaro, M. Bearpark, J. J. Heyd, E. Brothers, K. N. Kudin, V. N. Staroverov, R. Kobayashi, J. Normand, K. Raghavachari, A. Rendell, J. C. Burant, S. S. Iyengar, J. Tomasi, M. Cossi, N. Rega, J. M. Millam, M. Klene, J. E. Knox, J. B. Cross, V. Bakken, C. Adamo, J. Jaramillo, R. Gomperts, R. E. Stratmann, O. Yazyev, A. J. Austin, R. Cammi, C. Pomelli, J. W. Ochterski, R. L. Martin, K. Morokuma, V. G. Zakrzewski, G. A. Voth, P. Salvador, J. J. Dannenberg, S. Dapprich, A. D. Daniels, O. Farkas, J. B. Foresman, J. V. Ortiz, J. Cioslowski and D. J. Fox, *Gaussian09 Revision A.01*, Gaussian Inc., Wallingford CT, 2009.
29 M. Rätsep, Z.-L. Cai, J. R. Reimers and A. Freiberg, *J. Chem. Phys.*, 2011, **134**, 01B608.
30 Y. Niu, Q. Peng, C. Deng, X. Gao and Z. Shuai, *J. Phys. Chem. A*, 2010, **114**, 7817.
31 Q. Peng, Q. Shi, Y. Niu, Y. Yi, S. Sun, W. Li and Z. Shuai, *J. Mater. Chem. C*, 2016, **4**, 6829.
32 H. Ma, W. Shi, J. Ren, W. Li, Q. Peng and Z. Shuai, *J. Phys. Chem. Lett.*, 2016, **7**, 2893.
33 T. Lu and F. W. Chen, *J. Comput. Chem.*, 2012, **33**, 580.
34 Y. Hong, J. W. Lam and B. Z. Tang, *Chem. Soc. Rev.*, 2011, **40**, 5361.

35 J. Gibson and T. Penfold, *Phys. Chem. Chem. Phys.*, 2017, **19**, 8428.
36 J. Gibson, A. P. Monkman and T. J. Penfold, *ChemPhysChem*, 2016, **17**, 2956.
37 M. K. Etherington, J. Gibson, H. F. Higginbotham, T. J. Penfold and A. P. Monkman, *Nat. Commun.*, 2016, **7**, 13680.
38 Dalton, A Molecular Electronic Structure Program, http://daltonprogram.org.
39 R. Ishimatsu, S. Matsunami, K. Shizu, C. Adachi, K. Nakano and T. Imato, *J. Phys. Chem. A*, 2013, **117**, 5607.